Journal of Alloys and Compounds 797 (2019) 1078–1085

Contents lists available at ScienceDirect

Journal of Alloys and Compounds

journal homepage: http://www.elsevier.com/locate/jalcom

Thermoelectric properties improvement in Mg_2Sn thin films by structural modification

Mahsasadat Safavi [a, *], Nicolas Martin [b], Vincent Linseis [c], Frank Palmino [a], Frederic Cherioux [b], Alain Billard [a], Mohammad Arab Pour Yazdi [a]

[a] Institut FEMTO-ST, UMR 6174, CNRS, Univ. Bourgogne Franche-Comté, UTBM, Site de Montbéliard, 90010 Belfort, France
[b] Institut FEMTO-ST, UMR 6174, CNRS, Univ. Bourgogne Franche-Comté, 15B, Avenue des Montboucons, 25030 Besançon, France
[c] Linseis Messgeräte GmbH, Vielitzer Str. 43, 95100 Selb, Germany

ARTICLE INFO

Article history:
Received 6 March 2019
Received in revised form
16 May 2019
Accepted 17 May 2019
Available online 18 May 2019

Keywords:
Mg_2Sn
Thin film
Sputtering
Thermoelectric properties
Thermal stability

ABSTRACT

Mg-Sn thin films ($21 \leq$ at. % Sn ≤ 42.5) were deposited by magnetron sputtering in the argon atmosphere. The structure and morphology of the films were characterized as a function of the composition. Mg_2Sn structure was changed from stable face-centered cubic to metastable orthorhombic structure while the content of Sn in the films increased. The influence of this structural modification on thermoelectric properties was discussed in a wide range of temperatures (30–200 °C). The film carrier concentration and mobility were measured to explain the electronic transport behavior as a function of the film structural modifications. The maximum figure of merit ZT ≈ 0.26 at 200 °C was reached for the film with 36 at. % Sn while a mixture of cubic and orthorhombic Mg_2Sn structures coexisted. An annealing treatment was performed under vacuum (~10^{-4} Pa) at different temperatures (up to 600 °C) to determine the limit of structural and morphological stability of this film.

1. Introduction

Thermoelectric materials have attracted global interest according to their ability to convert directly thermal to electrical energy, thus providing a clean and renewable supply of energy [1]. The efficiency of thermoelectric materials refers to their dimensionless figure of merit (ZT), defined by equation (1):

$$ZT = \frac{PF}{K}T \quad (1)$$

$$\text{with } PF = \alpha^2\sigma \quad (2)$$

where *PF* is the thermoelectric power factor (W m^{-1} K^{-2}), α the Seebeck coefficient (μV K^{-1}), σ the electrical conductivity (Ω^{-1} m^{-1}), *K* the thermal conductivity (W m^{-1} K^{-1}) and *T* the absolute temperature (K). As a result, a good thermoelectric power factor (*PF*) as defined by equation (2) and a low thermal conductivity (K) lead to a high ZT value [2]. Nowadays, Mg_2X (X = Si, Sn, Ge) semiconductor compounds and their solid solutions have drawn more attention due to their thermal stability, low cost, none toxicity, constituent abundance in the earth's crust, environmentally friendly, low density and providing both n and p-type conductions [3]. Most of the studies about Mg_2X compounds are limited to n-type materials and development of p-type compounds is still a challenging task. Song et al. [4] have determined a ZT value of about 0.02 at 147 °C for un-doped Mg_2Sn (with cubic structure), prepared by bulk mechanical alloying and hot-pressing method. Chen and Savvides [5] have doped Mg_2Sn by Ag using a modified vertical Bridgman method. As a result, the maximum *PF* value they have obtained was 4×10^{-3} $Wm^{-1}K^{-2}$ for sample with 2 at. % Ag at 147 °C. Chen et al. [6] have pointed out the maximum ZT of about 0.30 for 0.5 at. % Ag-doped Mg_2Sn ingot at 200 °C, which was prepared by using a rocking Bridgman furnace. Le-Quoc et al. [7] have reported a high *PF* value of about 5×10^{-3} $Wm^{-1}K^{-2}$ at room temperature for stoichiometric Mg_2Sn thin film doped with 1 at.% Ag, deposited by co-sputtering assisted by multi-dipolar microwave plasma. Choi et al. [8] have obtained maximum ZT = 0.18 at 327 °C for a p-type system of Ag-doped Mg_2Sn bulk sample by employing vacuum melting method and spark plasma sintering (SPS) process which is comparable to the value for an n-type system of Mg_2Si. An et al. [9] have reported a power factor of 1.4×10^{-3} $Wm^{-1}K^{-2}$ for

* Corresponding author.
E-mail address: mahsasadat.safavi@utbm.fr (M. Safavi).

https://doi.org/10.1016/j.jallcom.2019.05.214
0925-8388/

1 mol.% Ag-doped Mg_2Sn (Mg:Sn = 67:33), as much as 10 times bigger than un-doped Mg_2Sn, using SPS method. Varma et al. [10] have employed radio frequency induction casting method under Ar atmosphere for developing high quality un-doped and silver-doped Mg_2Sn. The ZT value reached about 0.055 at 50 °C for Mg excess concentration sample doped by Ag (authors named this sample 10.8 Mg (0.3Ag)).

As shortly described, many works were focused on bulk materials, while development of thin film materials with optimized ZT are required to reduce the size of current thermoelectric devices in order to address them in miniaturized applications like Micro Electronic and Mechanical Systems (MEMS) [11] and Internet of Things (IoT) [12]. Different methods were suggested for producing thermoelectric thin films such as flash evaporation [13], pulsed laser deposition (PLD) [14,15], electrochemical deposition [16], metal organic chemical vapor deposition (MOCVD) [17], sputtering [18–21], molecular beam epitaxy (MBE) [22]. Among these techniques, sputtering has numerous advantages such as good reproducibility, easy way to control the film composition and homogeneity, environmentally friendly and so on [23,24].

In this study, Mg-Sn thin films (21 ≤ at. % Sn ≤ 42.5) were synthesized by co-sputtering of Mg and Sn targets in an argon atmosphere. In a first part, structure and morphology of the films were characterized as a function of the film composition. By adjusting the Sn content in the films, it becomes possible to change the Mg_2Sn structure from stable cubic to metastable orthorhombic structure. In the second part, the influence of this structural modification on thermoelectric properties of the films was discussed as a function of temperature and the electronic transport properties were considered to understand the film electrical resistivity variation.

2. Materials and methods

2.1. Thin film deposition

Mg-Sn coatings were synthesized by co-sputtering of Mg (purity 99.9 at. %, ∅ 50 mm × 3 mm) and Sn (purity 99.9 at. %, ∅ 50 mm × 3 mm) targets in an argon atmosphere. The reactor was a 90 L cylinder Alcatel 604 SCM (CIT Alcatel, Annecy, France) pumped down via a turbo molecular pump system that permitted a residual vacuum below 10^{-4} Pa. The chamber was equipped with circular planar and water-cooled magnetron sputtering sources and the rotating substrate holder was parallel to these sources at about 60 mm. The targets of Mg and Sn were located 140 mm from each other. The Mg and Sn targets were supplied with a pulsed DC (Direct Current) Advanced Energy dual generator authorizing the control of the discharge power. The latter was fixed at 70 W for Mg target and was systematically changed on Sn target from 25 to 52 W to tune the coating composition. Argon flow rate was controlled with a Brooks flowmeter and the working pressure was kept at 0.41 Pa during deposition (working pressure measured using a MKS Baratron gauge). Special chip (second-generation chip) produced by Linseis (Supplementary data, Fig. S1), as well as fused quartz and glass microscope slides (76 mm × 26 mm × 2 mm) were used as substrates. Before each set, glass microscope slides and fused quartz were cleaned with alcohol, soap and then rinsed with water. The substrates were placed on the substrate holder at 60 mm from the substrate holder axis and all depositions were carried out at floating temperature ($T_{substrate}$ < 70 °C). The main sputtering parameters are summarized in Table 1.

2.2. Characterization devices

The structural characterization of coatings was performed by Bragg-Brentano configuration X-ray diffraction (XRD) using a BRUKER D8 focus diffractometer with a cobalt X-ray tube ($Co_{K\alpha1+\alpha2}$ radiations λ = 0.178897 nm) and equipped with a LynxEye linear detector. Diffractograms were collected under air during 10 min in the 20–80° 2θ angle range at a scan rate of 0.1°s^{-1}. The morphology of the coatings on brittle fracture cross-section and on their top surface were observed by a Jeol JSM 7800F Field Emission Gun Scanning Electron Microscope (FEG-SEM). The chemical composition was determined by Energy-Dispersive X-ray Spectroscopy (EDS). The film's thickness was measured by step method with an Altysurf Profilometer (Altisurf 500) manufactured by Altimet society. Before each measurement, the calibration of the experimental device was realized with a reference sample number 787569 accredited by CETIM organization. DC electrical resistivity, free carrier concentration and mobility were performed under air in the temperature range 30–200 °C for the films deposited on glass slides by means of a homemade system based on the van der Pauw method. In order to warrant the ohmic behavior of the four contacts, I-V curves were systematically plotted, and the linear evolution was checked for all van der Pauw combinations. Two cycles of measurements were carried out on each sample. The first cycle started at 30 °C and the sample was heated up to 200 °C with a ramp of 2 °C min^{-1} followed by 10 min stabilization at 200 °C. Afterward, the temperature was decreased with the same ramp down to 30 °C and the second cycle continued with the same temperature profile as the first cycle. For charge carrier's mobility and concentration, a magnetic field of 0.8 *T* was perpendicularly applied to the sample surface.

Thin Film Analyzer (TFA) designed by Linseis Co. was used to measure under vacuum all thermoelectric properties on the same sample and in one measurement run in order to calculate in-plan ZT value (Supplementary data, Fig. S2). TFA employed the 3ω technique at quasi-steady state conditions for determining the thermal conductivity. It is also able to get resistivity by a 4-point van der Pauw method for measurement of electrical transport properties. Seebeck coefficient of the films was also measured from the magnitude of an induced thermoelectric voltage in response to a temperature difference across the films. In TFA, the Seebeck coefficient of the film was obtained using the following equation:

$$S - S_{Pt} = \frac{-V_{Th}}{\Delta T} = \frac{(-V_{Hot} - V_{Cold})}{T_{Hot} - T_{Cold}} \quad (3)$$

where V_{Th} is the thermovoltage (μV), Δ*T* the temperature gradient between the voltage measurement contacts (K) and S_{Pt} the Seebeck coefficient of the platinum contacts (μVK^{-1}).

By plotting the evolution of measured thermovoltage *vs.* applied temperature gradient, the slope can be considered as the Seebeck coefficient. More details of TFA setup are reported by Linseis et al.

Table 1
Sputtering parameters used during deposition of Mg_2Sn coatings.

Target	Discharge Power (W)	Frequency (kHz)	T_{off} (μs)	Ar Flow Rate (sccm)	Working Pressure (Pa)	Run Duration (min)	Draw Distance ($D_{T\text{-}S}$) (mm)
Sn	25–52	50	4	50	0.41	20	60
Mg	70						

[25].

In order to get a stabilization of the film's properties, all measurements related to thermoelectric properties were carried out in three cycles consisting of a heating and cooling run in the temperature range from 30 °C to 200 °C under vacuum at about 10^{-4} Pa. In each cycle of measurement, the sample was heated with a ramp of 2 °C min^{-1} and was remained at a given temperature for 2 min (Supplementary data, Fig. S3). Afterward the temperature decreased with the same ramp down to 30 °C. The second and third cycles continued with the same temperature profile as the first cycle. The films electrical conductivity, thermal conductivity and Seebeck coefficient were recorded for each 10 °C step. After three-cycles of measurements (heating and cooling cycles) films were completely educated (Supplementary data, Table S1). To avoid some confusing data, in this work, only the results collected for the third cycle of cooling were reported.

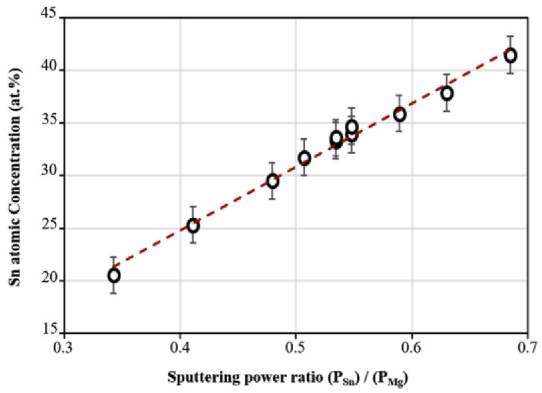

Fig. 1. Evolution of the Sn atomic concentration in the films measured by Energy-Dispersive X-ray Spectroscopy (EDS) vs. sputtering power ratio applied to each target. The red dotted line is a guide for the eye. (For interpretation of the references to colour in this figure legend, the reader is referred to the Web version of this article.)

3. Results and discussion

Fig. 1 shows the evolution of the atomic concentration of Sn measured by EDS analyses for each coating deposited on fused quartz as a function of the power ratio applied to each target (P_{Sn}/P_{Mg}) during the sputtering process. Three different zones of each coating were selected for EDS measurements and the average concentration was calculated. It can be noted that EDS analyses show relatively homogenous composition on the entire surface of deposited thin films (Supplementary data, Fig. S4). These results show that as the power ratio applied to each target (P_{Sn}/P_{Mg}) increases, films become Sn-rich following a linear evolution.

Fig. 2 presents the X-ray diffraction patterns of as-deposited coatings with different atomic concentrations of Sn. The XRD results indicate that for coatings containing 21 ≤ at. % Sn ≤ 25, face-centered cubic (fcc) Mg_2Sn structure coexists with secondary phase of Mg with hexagonal close-packed (hcp) structure related to (002) diffracted peak at 2θ ≈ 41°.

For coatings containing 30 at. % up to 33.5 at. % Sn, the hcp Mg phase vanishes and well-crystallized stable fcc Mg_2Sn structure is obtained. For coatings with 35 ≤ at. % Sn ≤ 37.4, measurements of (211) diffracted signal at 2θ ≈ 28.05° confirms the presence of a metastable orthorhombic Mg_2Sn structure in addition to the fcc Mg_2Sn structure. In this range of compositions and because of orthorhombic and cubic structures coexistence, the Full Width at Half Maximum (FWHM) of the peaks increases, which corresponds to films with a poor crystallized state. Samples containing 37.6 ≤ at. % Sn ≤ 38, are crystallized in metastable orthorhombic structure (jcpds 00-031-0812) with no diffraction peaks related to the fcc structure. Finally, for coatings with 39.5 ≤ at. % Sn ≤ 42.5

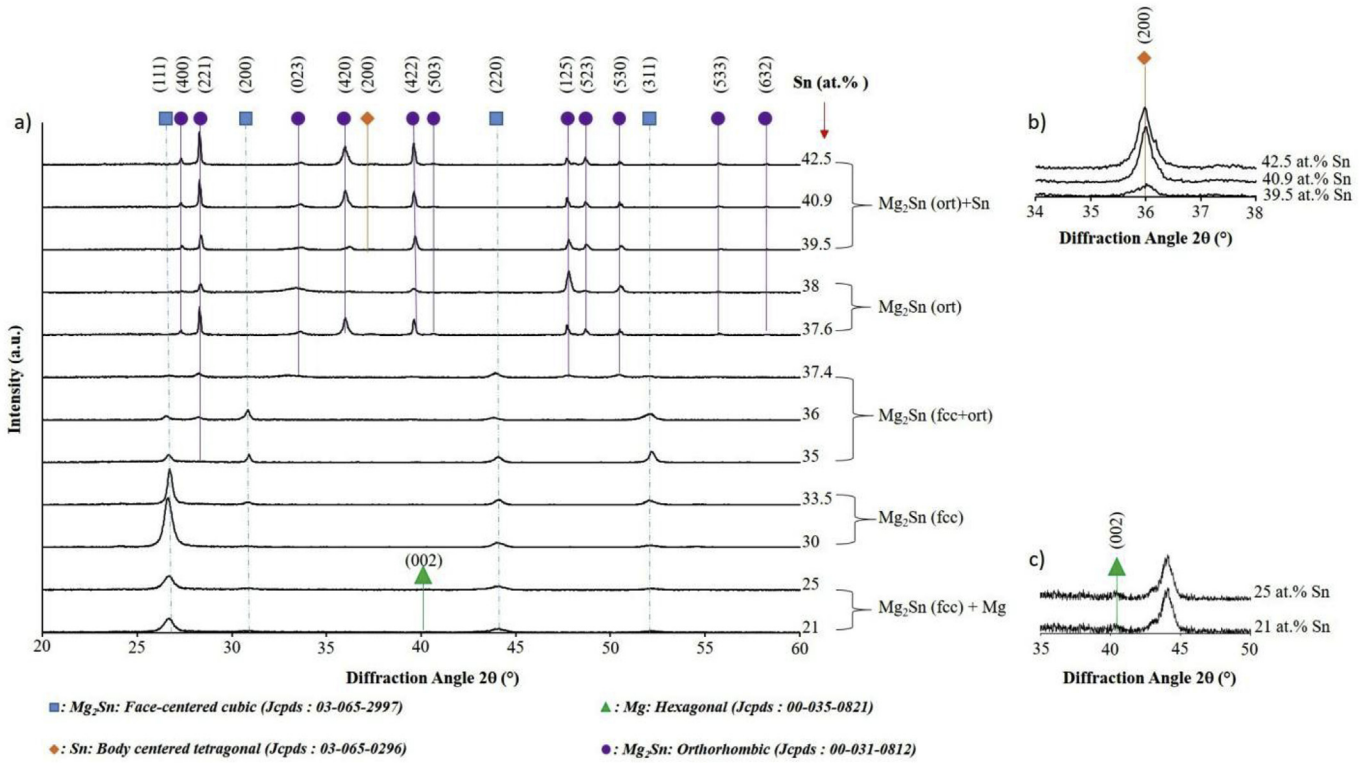

Fig. 2. a) XRD patterns of Mg-Sn coatings deposited on glass substrate as a function of the atomic concentration of Sn. Magnification at b) 2θ = 34°–38° and c) 2θ = 35°–50°.

metastable orthorhombic Mg_2Sn co-exists with the body centered tetragonal (bct) Sn phase as shown from the (200) diffracted signal at $2\theta \approx 35.7°$.

Since the sample with 36 at. % of Sn presents a mixture of cubic and orthorhombic structures, this sample was selected and annealed under vacuum of about 10^{-4} Pa at different temperatures for 2 h. Such treatments were performed to understand until which temperature the coexistence of orthorhombic and cubic structures could be maintained stable and to determine the limit of Mg_2Sn structure decomposition under vacuum. Fig. 3 shows the XRD patterns of this film annealed up to 600 °C. Until 300 °C, the cubic Mg_2Sn structure coexists with the (211) diffracted peak related to the metastable orthorhombic Mg_2Sn phase. For temperatures in-between 350-500 °C, the metastable orthorhombic phase disappears and the well-crystallized stable cubic Mg_2Sn structure is obtained. As this sample has a non-stoichiometric composition (Sn-rich content) in the temperature above 350 °C, the excess of Sn begins to release with the appearance of Sn secondary phase ((200) diffracted signal related to Sn phase is detected at $2\theta \approx 37°$). For temperatures higher than 500 °C, the cubic Mg_2Sn structure vanishes (decomposition of Mg_2Sn phase leading to Mg and Sn formation). The (200) diffracted signal related to Sn phase (jcpds 03-065-0296) coexists with (100) and (110) diffracted peaks of Mg related to hcp and bcc phases, respectively.

Top surface morphology observations by SEM of thin films deposited on glass substrate are shown in Fig. 4. As-deposited Mg-Sn coatings with Sn content of 21 at. % up to 42.5 at. % were selected. It is evident that all as-deposited films perfectly cover the surface of the substrate and no cracks and delamination were detected on top surface of the films. The films with 21 at. % Sn up to 33.5 at. % Sn reveal a granular morphology with a lateral grain size ranging from 130 nm (film with 21 at. % Sn) to about 70 nm (film with 33.5 at. % Sn). It can be observed in Fig. 4 that the separated granular morphology becomes more compact with a lower porosity while Sn content increases. Films obtained with a higher concentration of Sn ($35 \leq$ at. % Sn ≤ 38) present a cone-like shape microstructure. Looking at the morphology of the films with 38 at. % Sn, smooth surface with cone-like shape microstructures co-exist, especially for this sample. Finally, the film morphology returns to granular form with rising of Sn content to about 42.5 at. %. As a result, increasing Sn content in the film as the structure changes from cubic to orthorhombic, the granular morphology becomes more and more compact. For the films with a mixture of cubic and orthorhombic structures (35–36 at. % Sn), cone-like morphologies are observed while in the case of the film with Sn $\geq$ 38 at.% (well-crystallized in orthorhombic structure), the morphology becomes completely compact.

Fig. 5 reveals brittle fracture cross section observations of the films as a function of the Sn atomic concentration. It can be seen that coatings containing $21 \leq$ at. % Sn ≤ 25 present a porous granular aspect compared to other samples. By increasing the atomic concentration of Sn until 30–35 at. %, the morphology changes to slight columnar and becomes denser. The coating with 36 at. % Sn exhibits a relatively dense columnar morphology with submicron in-plan featured sizes. The coatings containing $38 \leq$ at. % Sn ≤ 42.5 show a completely dense and compact morphology. No cracks are detected and a good adhesion between coating and substrate is observed. It is well known that, regarding to high energy of sputtered atoms, adhesion of the films deposited by sputtering is much better than those obtained with other deposition methods, e.g. by

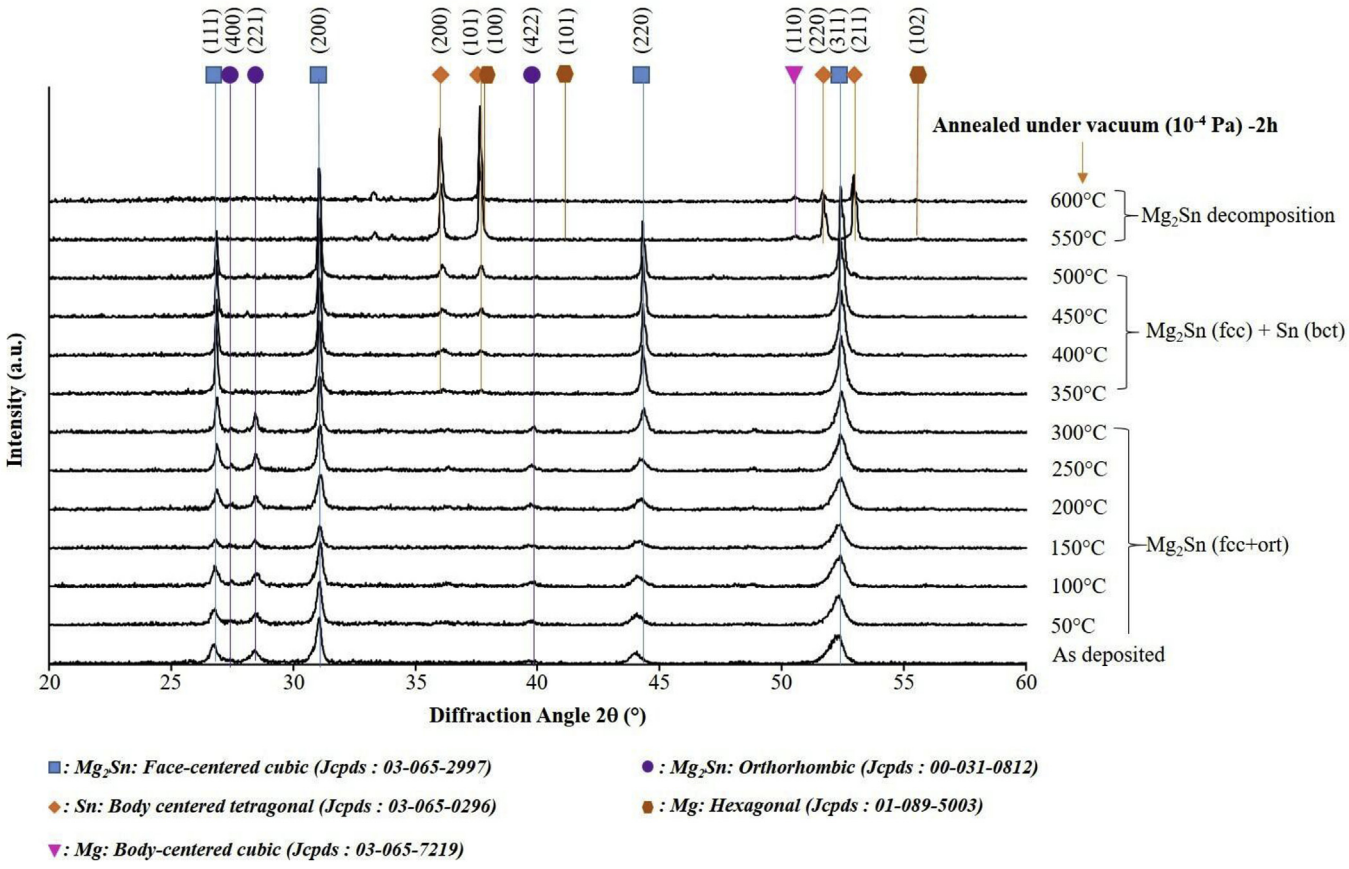

Fig. 3. X-ray diffraction patterns of the film with 36 at. % Sn deposited on glass substrate and post annealed under vacuum (10^{-4} Pa) for 2 h at different temperatures.

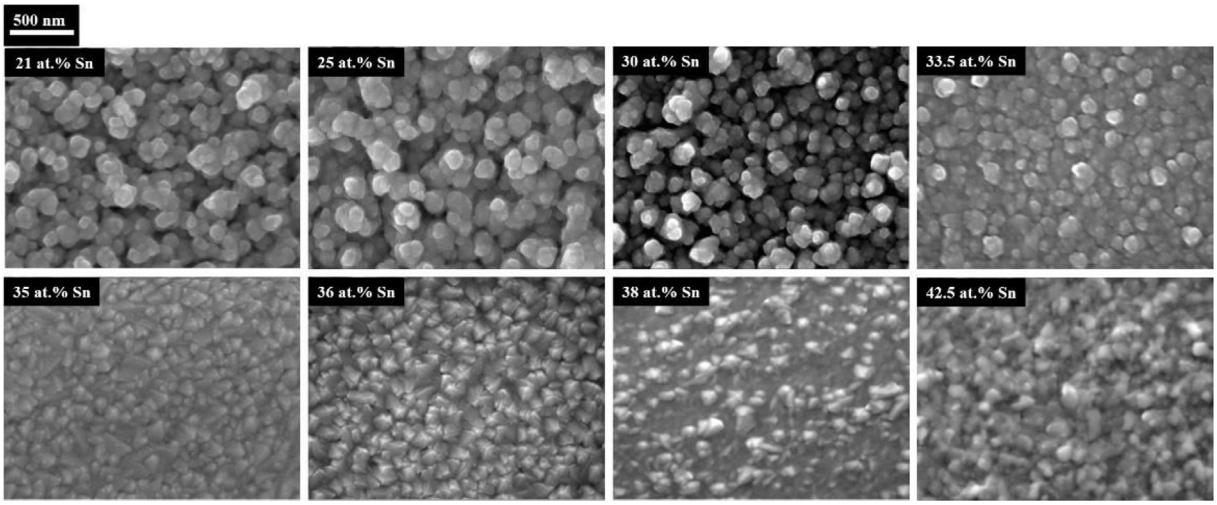

Fig. 4. SEM micrographs of as-deposited Mg-Sn films on glass substrate: Top surface images vs. composition.

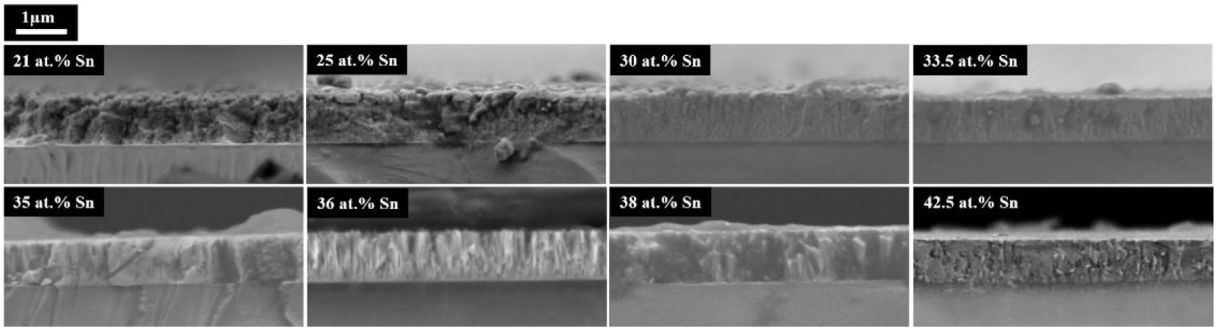

Fig. 5. SEM cross section micrographs vs. composition of Mg-Sn thin films deposited on glass substrate.

thermal evaporation [7]. The thickness of the films measured by SEM is relatively homogeneous with an average of about 1 μm. This value is in good agreement with those measured by profilometry.

Fig. 6 shows the top surface observation (a) and X-ray mapping (b) of the film with 36 at. % Sn deposited on a glass substrate after 2 h annealing at 600 °C under vacuum (10^{-4} Pa). It is noticeable that the film morphology completely changed. Sn atoms segregated from Mg_2Sn layer and an entirely film decomposition happened. As confirmed by X-ray mapping image heterogeneous Sn and Mg areas are formed. This result is in good agreement with XRD patterns of this sample after an annealing at the temperature above 500 °C (Fig. 3).

Fig. 7 shows the electronic transport properties of Mg-Sn thin films *vs.* temperature measured under air. Fig. 7a illustrates the dependency of DC electrical resistivity of the films with Sn content of 33.5 at. % up to 42.5 at. % as a function of the temperature. As shown for the films with 33.5 at. % Sn, which are well-crystallized in fcc Mg_2Sn structure, the electrical resistivity decreases as the temperature rises. It is well known that the electrical resistivity of semiconductor materials decreases with increasing temperature [26]. For the films with 35 ≤ at. % Sn ≤ 37.6, where the crystal structure changes from cubic to orthorhombic structure, the variation of electrical resistivity becomes quite constant as a function of the temperature. For the coatings containing 39.5 ≤ at. % Sn ≤ 42.5 with the orthorhombic structure and presence of Sn secondary phase, the electrical resistivity is enhanced by the temperature, that is associated to a metallic-like behavior. It is related to the excess of Sn atoms. It is important to note that, especially for the sample with 36 at. % Sn, the electrical resistivity remains relatively constant *vs.* temperature (between 30 °C and 200 °C) with a value of about $2.31 \times 10^{-5}\ \Omega$ m.

The variation of carrier concentration *vs.* temperature for the film with different Sn concentrations is shown in Fig. 7b. It is important to highlight that the film carrier concentration increases with Sn content in the films. Liu et al. [27] reported the influence of intrinsic point defects on electronic transport properties of Mg_2X (X = Si, Ge, Sn) systems. They showed that Mg vacancies and interstitial Mg are assumed to be the main defects in Mg_2X compounds according to their relatively low formation energies. Mg vacancies and interstitial Mg behave as acceptor and donor sites, respectively. We suppose that the increase of carrier concentration in Mg_2Sn films, while Sn content rises, can be explained by the formation of Mg vacancies. The carrier concentration for all coatings is enhanced by increasing the temperature and reaches the highest values (more than $10^{27}\ m^{-3}$) for the films containing 42.5 at. % Sn (order of magnitude of carrier concentrations in metals).

Fig. 7c shows the variation of carrier mobility of the films *vs.* temperature. The carrier mobility of all films decreases while the temperature rises. The carrier mobility is relatively low for the films adopting the Mg_2Sn cubic structure (33.5 at. % Sn). As the formation of metastable orthorhombic Mg_2Sn begins, carrier mobility increases (35 ≤ at. % Sn ≤ 37.6) and the highest carrier mobility is obtained for the single phase orthorhombic Mg_2Sn with 37.6 at. % Sn. Finally, a further increase of the Sn content (≥39.5 at. %) leads to a drastic decrease of the film carrier mobility. It is assigned to the

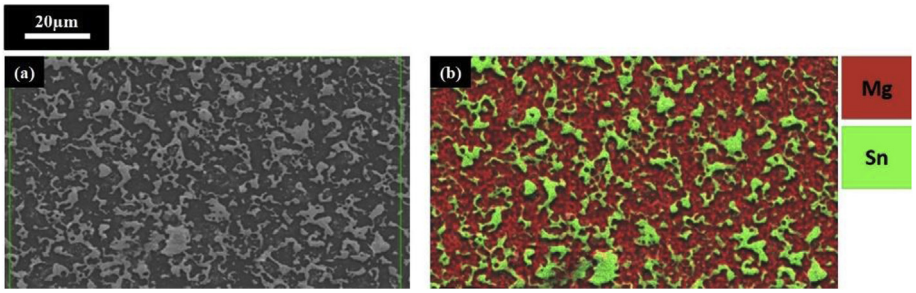

Fig. 6. (a) Top surface observation and (b) X-ray mapping of the film with 36 at. % Sn deposited on glass substrate after 2 h annealing at 600 °C under vacuum (10^{-4} Pa).

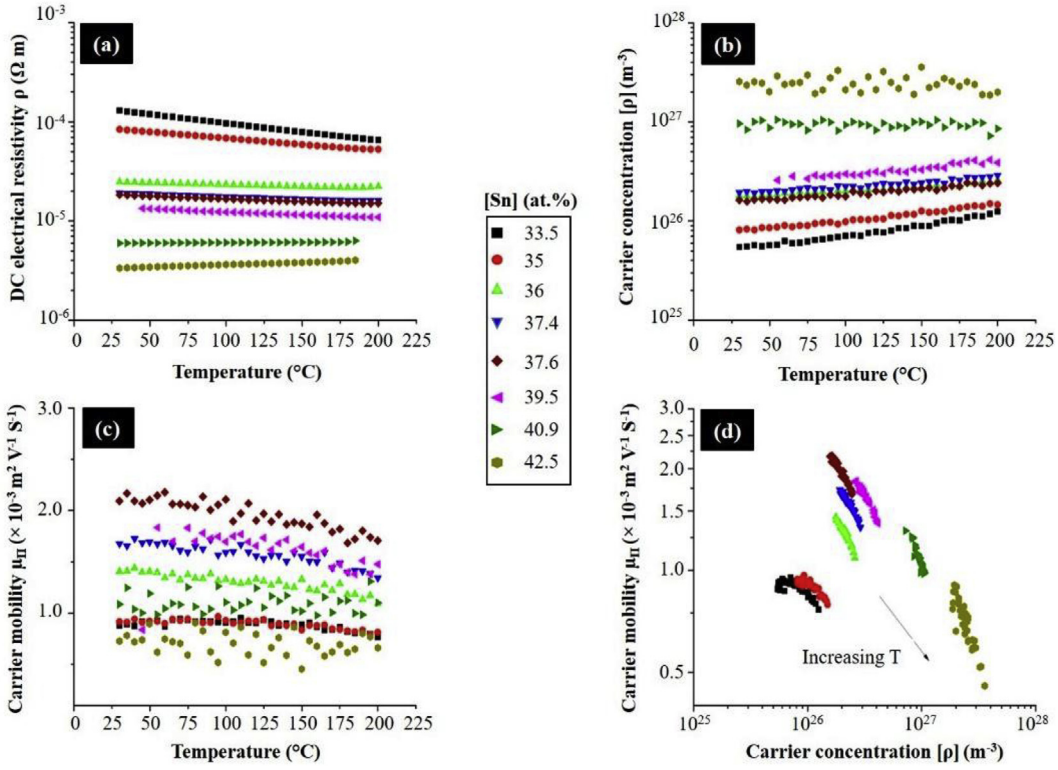

Fig. 7. Electronic transport properties of MgSn thin films measured by Hall Effect under air. a) DC electrical resistivity, b) carrier concentration, c) and carrier mobility vs. temperature, d) carrier mobility vs. carrier concentration.

presence of secondary Sn phase in these samples as detected by XRD patterns (Fig. 2).

Fig. 7d reveals the variation of carrier mobility as a function of the carrier concentration. For all films, this ratio decreases by increasing the temperature. It is clear that the highest ratios of carrier mobility to carrier concentration are obtained for the films exhibiting the orthorhombic structure. With the presence of Sn secondary phase in the films with at. % Sn $\geq$ 39.5, this ratio starts to decrease and the films tend to behave like a metallic compound.

The thermoelectric properties were measured under vacuum (about 10^{-4} Pa) at different temperatures using TFA device on Linseis chips covered by Mg-Sn thin films (Fig. 8). The film electrical conductivity decreases by increasing the atomic concentration of Sn from 21 to 33.5 at. % (Mg_2Sn fcc structure). Then, the films conductivity enhances while the concentration of Sn increases up to 42.5 at. % and the crystal structure changes to orthorhombic Mg_2Sn structure (Fig. 8a). Both samples with an excess of Mg or Sn show the highest values of electrical conductivity (films with Sn = 21 at. % and Sn = 42.5 at. %, respectively). An et al. [6] reported an electrical conductivity close to 10^4 Sm^{-1} for bulk Mg_2Sn (67:33) at 50 °C. At the same temperature, the electrical conductivity of about 2×10^4 Sm^{-1} was obtained in the present work for the film with 36 at.% Sn.

Fig. 8b shows the variations of Seebeck coefficient *vs.* temperature. For all coatings, Seebeck coefficient is positive throughout the measured temperature range. All films are p-type semiconductors [28]. The Seebeck coefficient and carrier concentration are inversely proportional. Therefore, as the carrier concentration rises, the Seebeck coefficient decreases [9]. With respect to Le-Quoc et al. [29], the films with lower atomic concentration of Sn, exhibits lower Seebeck coefficient and higher electrical conductivity. At room temperature, the Seebeck coefficient varies from 2.1 μVK^{-1} to 174 μVK^{-1} for films with different contents of Sn. The value reported for the Seebeck coefficient in bulk Mg_2Sn (while the Mg to Sn atomic ratio is 2:1) is about 120 μVK^{-1} at 30 °C [5]. The best Seebeck coefficient obtained in the present work is about 120 μVK^{-1} at 30 °C for the film with 36 at. % Sn. The films containing secondary phases of Mg or Sn show relatively low Seebeck values

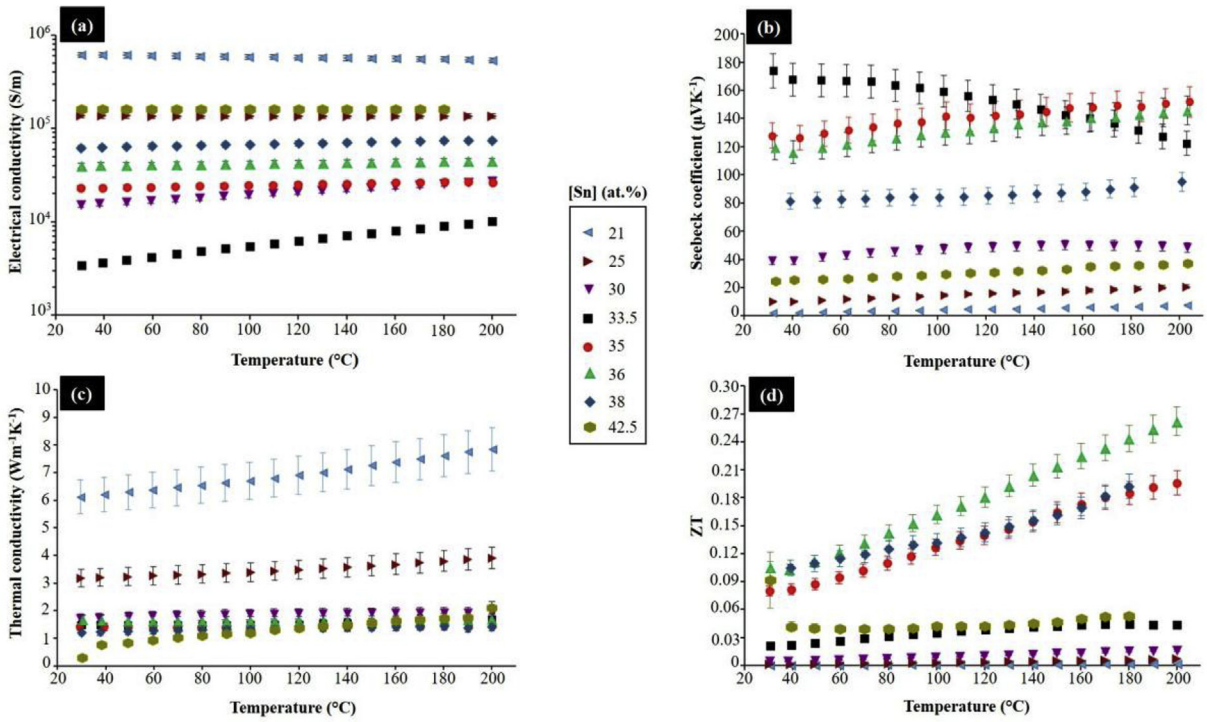

Fig. 8. Thermoelectric properties of the films deposited on Linseis chips and measured by TFA system under vacuum (10^{-4} Pa) vs. temperature. (a) Electrical conductivity, (b) Seebeck coefficient, (c) thermal conductivity and (d) figure of merit ZT vs. temperature.

compared to single phase Mg_2Sn films. The coating with 35 ≤ at. % Sn ≤ 36 and containing a mixture of cubic and orthorhombic structures exhibits the highest Seebeck coefficient (152 μV K^{-1}) at high temperature. The sample with cubic structure (at. % Sn ≈ 33.5) present the highest value of Seebeck coefficient (174 μV K^{-1}) at low temperature and while temperature rises, the coefficient decreases.

Fig. 8c represents the evolution of thermal conductivity of thin films *vs*. temperature. It is clear that while eliminating the secondary phase of Mg and rising Sn concentration, the thermal conductivity significantly reduces. The highest thermal conductivity is related to the coating containing 21 at. % Sn (7.9 W m^{-1} K^{-1}). The thermal conductivity for coating with 42.5 at. % Sn is more affected by the variation of temperature. As previously noted, lower thermal conductivity value can be expected for deposited thin films with polycrystalline structure compared to the same materials in bulk form. Chen and Savvides [30] reported a thermal conductivity of about 5–15 $Wm^{-1}K^{-1}$ for bulk Mg_2Sn. The obtained thermal conductivity of the present work is 1.4 $Wm^{-1}K^{-1}$ for the film with 36 at. % Sn, which is at least 3 times less than bulk Mg_2Sn. With respect to results of SEM morphological observations (Figs. 4 and 5), as the content of Sn in the films increases, a denser morphology is obtained and it is well known that a denser morphology leads to a lower thermal conductivity due to phonon scattering phenomenon [7,18].

Fig. 8 d indicates the variation of figure of merit (ZT) as a function of the temperature for Mg-Sn thin films.

The samples containing 21 at. % Sn up to 25 at. % Sn show low ZT values as they behave like metal compounds due to the presence of Mg secondary phase. By increasing the content of Sn from 30 at. % to 33.5 at. %, (samples with fcc structure and without secondary phase of Sn), ZT values slightly enhance but remain relatively stable *vs.* temperature. As the crystal structure changes from cubic to orthorhombic, (35 ≤ at. % Sn ≤ 38), the ZT values notably enhance and as shown in Fig. 8d, ZT increases with temperature. The maximum ZT value is obtained for thin films containing 36 at. % Sn with Mg_2Sn cubic and orthorhombic mixed crystal structures (ZT ≈ 0.26 at 200 °C). Choi et al. [8] reported ZT value < 0.025 for bulk Mg_2Sn (67:33) at the same temperature. The ZT slightly decreases for the film with 38 at. % Sn (with only the orthorhombic Mg_2Sn structure) and drops in the case of the film with 42.5 at. % Sn (orthorhombic Mg_2Sn structure + Sn secondary phase).

4. Conclusion

Mg-Sn thin films (21 ≤ at. % Sn ≤ 42.5) were deposited by magnetron co-sputtering. The film structure is affected by the Sn atomic concentration. Thin films containing 21 ≤ at. % Sn ≤ 25 have fcc Mg_2Sn structure with a secondary phase of Mg. The latter vanishes and fcc Mg_2Sn structure remains stable in the range of 30 ≤ at. % Sn < 33.5. Thin films with 35 ≤ at. % Sn ≤ 37.4 exhibit a mixture of cubic and orthorhombic Mg_2Sn phases. Films with 37.6 up to 38 at. % Sn adopt the orthorhombic Mg_2Sn structure. For the coatings containing 39.5 ≤ at. % Sn ≤ 42.5, orthorhombic Mg_2Sn structure with secondary phase of Sn co-exist. Thermal stability of the sample with cubic and orthorhombic mixed phases (thin film with 36 at. % Sn), was studied under vacuum. Until 300 °C, the mixed structure remains stable. The orthorhombic phase transforms to cubic while annealing temperature increases from 350 °C to 500 °C and the secondary phase of Sn begins to form. At temperatures higher than 500 °C, Mg_2Sn thin film completely decomposes into Mg and Sn. With formation of orthorhombic Mg_2Sn structure, ZT value is enhanced compared to that of the film with cubic Mg_2Sn structure. ZT values increase with temperature for orthorhombic Mg_2Sn coatings. The highest values of ZT = 0.26 is obtained at 200 °C while cubic and orthorhombic Mg_2Sn phases (36 at. % Sn) coexist in the films.

Conflicts of interest

The authors declare no conflict of interest. The founding sponsors had no role in the design of the study; in the collection, analyses, or interpretation of data; in the writing of the manuscript, or in the decision to publish the results.

Acknowledgements

The research was funded by “Région Bourgogne-Franche-Comté” and “Pays de Montbéliard Agglomération” (No. 2016Y-04501) in the frame of the MOBILITECH project.

Appendix A. Supplementary data

Supplementary data to this article can be found online at https://doi.org/10.1016/j.jallcom.2019.05.214.

References

[1] G.S. Polymeris, N. Vlachos, A.U. Khan, E. Hatzikraniotis, Ch. B. Lioutas, A. Delimitis, E. Pavlidou, K.M. Paraskevopoulos, Th. Kyratsi, Nanostructure and doping stimulated phase separation in high-ZT $Mg_2Si_{0.55}Sn_{0.4}Ge_{0.05}$ compounds, Acta Mater. 83 (2015) 285–293, https://doi.org/10.1016/j.actamat.2014.09.031.

[2] X. Zhang, L.D. Zhao, Thermoelectric materials: energy conversion between heat and electricity, J. Materiomics 1 (2015) 92–105, https://doi.org/10.1016/j.jmat.2015.01.001.

[3] C. Prahoveanu, A. Lacoste, S. Bechu, C. de Vaulx, K. Azzouz, L. Laversenne, Investigation of Mg_2(Si,Sn) thin films for integrated thermoelectric devices, J. Alloys Compd. 649 (2015) 573–578, https://doi.org/10.1016/j.jallcom.2015.07.043.

[4] R.B. Song, T. Aizawa, J.Q. Sun, Synthesis of $Mg_2Si_{1-x}Sn_x$ solid solutions as thermoelectric materials by bulk mechanical alloying and hot pressing, Mater. Sci. Eng. B 136 (2007) 111–117, https://doi.org/10.1016/j.mseb.2006.09.011.

[5] H.Y. Chen, N. Savvides, Microstructure and thermoelectric properties of n- and p-type doped Mg_2Sn compounds prepared by modified Bridgman method, J. Electron. Mater. 38 (7) (2009) 1056–1060, https://doi.org/10.1007/s11664-008-0630-1.

[6] H.Y. Chen, N. Savvides, T. Dasgupta, C. Stiewe, E. Mueller, Electronic and thermal properties of Mg_2Sn crystals containing finely dispersed eutectic structures, Phys. Status. Solidi. A 207 (2010) 2523–2531, https://doi.org/10.1002/pssa.201026119.

[7] H. Le-Quoc, A. Lacoste, E.K. Hlil, A. Bès, T. Tan Vinh, D. Fruchart, N. Skryabina, Thin films of thermoelecric compound Mg_2Sn deposited by co-sputtering assisted by multi-dipolar microwave plasma, J. Alloys Compd. 509 (2011) 9906–9911, https://doi.org/10.1016/j.jallcom.2011.07.085.

[8] S.M. Choi, T.H. An, W.S. Seo, C. Park, I.H. Kim, S.U. Kim, Doping effects on thermoelectric properties in the Mg_2Sn system, J. Electron. Mater. 41 (6) (2012) 1071–1076, https://doi.org/10.1007/s11664-012-1985-x.

[9] T.H. An, S.M. Choi, I.H. Kim, S.U. Kim, W.S. Seo, J.Y. Kim, C. Park, Thermoelectric properties of a doped Mg_2Sn system, Renew. Energy 42 (2012) 23–27, https://doi.org/10.1016/j.renene.2011.09.030.

[10] R.R. Varma, S.R. Kada, M.R. Barnett, Effect of magnesium and silver doping on the thermoelectric performance of cast Mg_2Sn alloys, J. Alloys Compd. 757 (2018) 142–149, https://doi.org/10.1016/j.jallcom.2018.05.054.

[11] C.A. Gould, N.Y.A. Shammas, S. Grainger, I. Taylor, Thermoelectric cooling of microelectronic circuits and waste heat electrical power generation in a desktop personal computer, Mater. Sci. Eng. B 176B (2011) 316–325, https://doi.org/10.1016/j.mseb.2010.09.010.

[12] J. Lopez, R. Rios, F. Bao, G. Wang, Evolving privacy: from sensors to the internet of things, Future Gener. Comput. Syst. 75 (2017) 46–57, https://doi.org/10.1016/j.future.2017.04.045.

[13] D. Zhao, M. Zuo, H. Geng, Enhanced thermoelectric performance of Ga-added $Bi_{0.5}Sb_{1.5}Te_3$ films by flash evaporation, Intermetallics 31 (2012) 321–324, https://doi.org/10.1016/j.intermet.2012.07.007.

[14] Y.F. Yamada, A. Ohtomo, M. Kawasaki, Parallel syntheses and thermoelectric properties of Ce-doped $SrTiO_3$ thin films, Appl. Surf. Sci. 254 (2007) 768–771, https://doi.org/10.1016/j.apsusc.2007.04.089.

[15] J. Chen, Y. Zhou, X. Ke, Y. Lv, Y. Li, S. Populoh, N. Chen, X. Shi, L. Chen, Y. Jiang, Electrical transportation performances of Nb-$SrTiO_3$ regulated by the anion related chemical atmospheres, Mater. Des. 97 (2016) 7–12, https://doi.org/10.1016/j.matdes.2016.02.066.

[16] K. Park, F. Xiao, B.Y. Rheem, N.V. Myung, Electrochemical deposition of thermoelectric Sb_xTe_y thin films and nanowires, J. Alloys Compd. 362 (2009) 362–364, https://doi.org/10.1016/j.jallcom.2009.05.106.

[17] H.W. You, S.H. Baek, K.C. Kim, O.J. Kwon, J.S. Kim, C. Park, Growth and thermoelectric properties of Bi_2Te_3 films deposited by modified MOCVD, J. Cryst. Growth 346 (2012) 17–21, https://doi.org/10.1016/j.jcrysgro.2012.02.033.

[18] Z. Zheng, P. Fan, J. Luo, G. Liang, H. Ma, X. Zhang, C. Yang, Y.Q. Fu, High-performance p-type inorganic-organic hybrid thermoelectric thin films, Nanoscale 10 (2018) 13511–13519, https://doi.org/10.1039/C8NR02065E.

[19] P. Bellanger, S. Gorsse, G. Bernard-Granger, C. Navone, A. Redjaimia, S. Vivès, Effect of microstructure on the thermal conductivity of nanostructured Mg_2(Si,Sn) thermoelectric alloys: an experimental and modeling approach, Acta Mater. 95 (2015) 102–110, https://doi.org/10.1016/j.actamat.2015.05.010.

[20] Z. Zheng, J. Luo, T. Chen, X. Zhang, G. Liang, P. Fan, Using high-thermal stability flexible thin film thermoelectric generator at moderate temperature, Appl. Phys. Lett. 112 (2018), https://doi.org/10.1063/1.5028390, 163901(1)-163901(5).

[21] M. Arab Pour Yazdi, N. Martin, C. Petitot, K. Neffaa, F. Palmino, F. Cherioux, A. Billard, Influence of sputtering parameters on structural, electrical and thermoelectric properties of Mg-Si coatings, Coatings 8 (2018) 380–395, https://doi.org/10.3390/coatings8110380.

[22] M.V. Daniel, M. Friedemann, J. Franke, M. Albrecht, Thermal stability of thermoelectric $CoSb_3$ skutterudite thin films, Thin Solid Films 589 (2015) 203–208, https://doi.org/10.1016/j.tsf.2015.05.024.

[23] M. Arab Pour Yazdi, P. Briois, F. Lapostolle, A. Billard, $SrZr_{1-X}Y_XO_3$ coatings by DC-magnetron sputtering, ECS Trans. 7 (1) (2007) 2313–2319, https://doi.org/10.1149/1.2729350.

[24] M. Arab Pour Yazdi, N. Fenineche, E. Aubry, A. Kiabi, A. Billard, Microstructure and magnetic properties of Ni_3Fe solid solution thin films deposited by DC-magnetron sputtering, J. Alloys Compd. 550 (2013) 252–257, https://doi.org/10.1016/j.jallcom.2012.09.136.

[25] V. Linseis, F. Völklein, H. Reith, K. Nielsch, P. Woias, Advance platform for the in-plane ZT measurement of thin films, Rev. Sci. Instrum. 89 (2018), https://doi.org/10.1063/1.5005807, 015110-015100-9.

[26] S. Lardjane, M. Arab Pour Yazdi, N. Martin, C. Bellourd, N.E. Fenineche, A. Schuler, G. Merad, A. Billard, Structural, electrical and magnetic characterization of in-situ crystallized ZnO: Co thin films synthesized by reactive magnetron sputtering, Mater. Chem. Phys. 161 (2015) 26–34, https://doi.org/10.1016/j.matchemphys.2015.04.037.

[27] X. Liu, L. XI, W. Qiu, J. Yang, T. Zhu, X. Zhao, W. Zhang, Significant roles of intrinsic point defects in Mg_2X (X= Si, Ge, Sn) thermoelectric materials, Adv. Electron Mater. 2 (2016) 1500284–1500294, https://doi.org/10.1002/aelm.201500284.

[28] Z.L. Du, H.L. Gao, J.L. Cui, Thermoelectric performance of quaternary $Mg_{2(1+x)}Si_{0.2}Ge_{0.1}Sn_{0.7}$ ($0.06 \leq x \leq 0.12$) solid solutions with band convergence, Curr. Appl. Phys. 15 (2015) 784–788, https://doi.org/10.1016/j.cap.2015.04.034.

[29] H. Le-Quoc, A. Lacoste, S. Béchu, A. Bès, D. Bourgault, D. Fruchart, Deposition of thin films of $Mg_2Si_{1-x}Sn_x$ solid solution by plasma-assisted co-sputtering, J. Alloys Compd. 538 (2012) 73–78, https://doi.org/10.1016/j.jallcom.2012.06.003.

[30] H.Y. Chen, N. Savvides, High quality Mg_2Sn crystals prepared by RF induction melting, J. Crys. Growth 312 (2010) 2328–2334, https://doi.org/10.1016/j.jcrysgro.2010.05.011.